

This is the submitted version of the article "Fatigue crack propagation behavior of a micro-bainitic TRIP steel", published in Materials Science and Engineering: A, 840, 2022, 142898.

<https://doi.org/10.1016/j.msea.2022.142898>

<https://www.sciencedirect.com/science/article/pii/S0921509322003069>

## **Fatigue crack propagation behavior of a micro-bainitic TRIP steel**

I. Burda<sup>1\*</sup>, K. Zweiacker<sup>1</sup>, A. Arabi-Hashemi<sup>1</sup>, P. Barriobero-Vila<sup>2</sup>, A. Stutz<sup>1</sup>, R. Koller<sup>1</sup>, H. Roelofs<sup>3</sup>, L. Oberli<sup>3</sup>, M. Lembke<sup>3</sup>, C. Affolter<sup>1</sup>, C. Leinenbach<sup>1</sup>

<sup>1</sup>Empa, Swiss Federal Laboratories for Materials Science and Technology, Dübendorf, Switzerland

<sup>2</sup>German Aerospace Center (DLR), Cologne, Germany

<sup>3</sup>Steeltec AG, Emmenbrücke, Switzerland

### **Abstract**

Controlling the grain size of steels is an effective way for tailoring their mechanical properties, such as yield strength, impact toughness, and ductility. In this study, a new industrial thermo-mechanical treatment was applied to a low-alloyed TRIP-assisted bainitic steel 13MnSiCr7 to achieve a substantial microstructural refinement. In this way the average grain size of the new micro-bainitic steel was decreased from ~25  $\mu\text{m}$  to ~5  $\mu\text{m}$ . Fatigue tests were carried out in order to investigate the influence of this new thermomechanical treatment on crack propagation behavior. Besides electron backscatter diffraction (EBSD), vibrating sample magnetometry (VSM), and high-energy synchrotron X-ray diffraction (HEXRD) were used to study the microstructure in the vicinity of the fatigue crack tip. The applicability of each method for detecting the martensitic transformation is discussed. In addition, the contribution of the latter to fracture toughness was assessed on the basis of the results obtained by HEXRD.

### **Keywords**

TRIP steel, grain refinement, fatigue crack propagation, high-energy synchrotron X-ray diffraction

# 1 Introduction

In the last two decades, a broad variety of advanced high strength steels (AHSS) has been developed, including the so-called TRansformation Induced Plasticity (TRIP) steels. Depending on their chemical composition and thermomechanical processing, the microstructure of these steels may consist of ferrite, bainite, martensite and residual austenite [1]. The key benefit of this type of steels is a combination of high strength and ductility, allowing the manufacturing of light-weight components with considerable energy absorption properties during impact.

Whereas classical TRIP steels found applications in flat products with modest strength and good formability, new TRIP-assisted bainitic steels with higher strength have gained an increasing interest for long products and automotive applications over the last decade. It was found that components manufactured out of TRIP-assisted bainitic steels often exhibit longer lifetimes under realistic cyclic load collectives comparing with conventional quenched and tempered (Q&T) steels [2]. When applying single overloads, the steel exhibits local hardening due to phase transformation from residual austenite to martensite. Consequently, the lifetime of the component is increased “in situ” [3,4]. This new class of steel can be produced from hot working temperatures applying natural cooling. Additional heat treatments like Q&T can be omitted, which eventually leads to reduction of costs and increased sustainability. However, the low cooling rate conditions in large components might cause coarse granular microstructure, which may lead to larger scatter of fatigue properties. This potential drawback can be avoided by reducing the hot deformation temperature during thermomechanical treatment in order to refine the prior austenite grains.

Recently, new industrial technologies in the production of hot rolled bars have allowed refinement of prior austenite grains in the order of few microns. In comparison with ferritic-pearlitic steels, the production of grain refined continuously cooled bainitic steels is not a trivial task. The small prior austenite grain size in combination with the available cooling schedule define the range of possible steel compositions. Typical commercially available continuously cooled bainitic steels do not fulfill these requirements. In the present work a steel alloy composition, namely 13MnSiCr7, was tailored allowing the production of the first micro-bainitic TRIP steel.

In real automotive steel parts under dynamic loads local plastic deformation might occur due to external overloads or stress concentrations (e.g. edges, notches, etc). Further cyclic loading, and the associated damage accumulation, may lead to fatigue crack initiation. At the same time, strain fields induced by the plastic deformation in the vicinity of crack tip may trigger the TRIP effect. Residual austenite partially transforms into martensite, and the resulting volume expansion introduces compressive stresses. The latter should restrict further crack growth, and,

as a consequence, the service life of the considered part increases. It is reasonable to believe that the spatial as well as size distribution of the residual austenite phase determines the magnitude of this effect [5].

From previous studies it is supposed that the refinement of the prior austenite grains also has a positive effect on the fatigue properties. Mughrabi and Höppel showed that Wöhler curves for materials with conventional and finer grain sizes differ [6]. In the range of high cycle fatigue (HCF) and low total strain, the fatigue behaviour is mainly determined by the strength of the material. Wöhler curves in this regime can be very well described with the Basquin approach. In the range of finite life (low cycle fatigue, LCF), the fatigue behaviour depends on ductility and on the ability of the material to withstand high cyclic strains.

Niendorf et al. [7–9] investigated the cyclic stability of a ferritic interstitial-free (IF) steel in the LCF range. Due to the high density of high-angle grain boundaries and the presence of fine grain boundary precipitates, cyclic softening was no longer observed after sufficient forming during strain-controlled cyclic testing. Additionally, a significant increase of the endurance limit was observed. One of the first investigations on the fatigue behaviour of fine-grained ferritic-pearlitic steels was done by Sawai et al [10]. Here, the endurance limit of the considered steel with a carbon content of 0.15 wt% could be increased by more than 50 %. Chapetti et al [11] confirmed this finding, but observed that small grains can lead to a higher notch sensitivity. On the other hand, the process of severe plastic deformation, which is used for the production of fine grained steels, might introduce local shear bands or cracks [12–16]. Therefore, phase transformations driven by thermal processes are often employed for the production of fine-grained steels. Investigations of cyclic properties of steels produced by severe plastic deformation are rare [17–19].

These mentioned research works considered ferritic-pearlitic microstructures and austenite grain sizes of one micrometer or below. However, prior austenite grain sizes of such dimensions are not compatible with the bainite transformation under industrial natural cooling conditions. In this case a prior austenite grain size in the order of five micrometer is considered to be more realistic and adequate.

In the present work, the fatigue crack propagation behaviour of TRIP-assisted bainitic steel 13MnSiCr7 in two processing conditions with different microstructures, particularly grain size, was studied. The reference steel 13MnSiCr7 [20] was conventionally hot rolled at 1100 °C. The new micro-bainitic steel was produced utilizing a thermomechanical hot rolling treatment designated XTP® [21,22]. The corresponding microstructural changes were studied by scanning electron microscopy (SEM), electron backscatter diffraction (EBSD), vibrating sample magnetometry (VSM) and high energy synchrotron X-ray diffraction (HEXRD). Finally, an assessment of the contribution of TRIP effect to the fracture toughness for both steels is discussed.

## 2 Materials and Methods

### 2.1 Material

Steel grade 13MnSiCr7 was industrially produced at Steeltec (80 ton heat, continuously casting 150x150 mm<sup>2</sup> billets and hot rolling bars). The nominal steel composition is given in Table 1. A low carbon content was chosen to achieve a high bainite content. Microalloying elements (Nb, V) were added to reach an acceptable high static strength level.

Table 1: Chemical composition of steel 13MnSiCr7.

Element	C	Si	Mn	S	Ni	Cr	Mo	V	Nb	Al	N
wt.%	0.14	0.53	1.75	0.01	0.07	0.64	0.01	0.09	0.06	0.03	0.011

The conventionally hot rolled reference bar (called “STD”) was 31 mm in diameter. During the rolling process a mean prior austenite grain size of ~25  $\mu\text{m}$  was achieved.

The refinement of microstructure of the STD material was achieved by subjecting the bars of reference steel to additional thermomechanical treatment. A new hot rolling technology, called XTP<sup>®</sup>, uses severe deformation in one single rolling step within a temperature window from 700 to 850°C to refine the austenite grains [20,21,23,24]. The schematic layout of the rolling line is shown in Figure 1. The first phase implies an induction heating of an input bar to the austenitization temperature of ~950°C. This is followed by isothermal holding for the temperature homogenization within the bar. The forming stage is carried out by means of a rolling mill, which consists of three cone-shaped rolls. The mill induces severe plastic deformation within the bar, leading to significant grain refinement of its microstructure. In this study, the cross-section of the bar was reduced by one single deformation step from initial Ø40 mm to Ø30 mm. After the forming stage the temperature of the bar was ~800°C. Under these conditions, a mean prior austenite grain size of ~5 $\mu\text{m}$  is expected. The micro-bainitic TRIP-assisted steel bar after thermomechanical treatment is hereafter referred to as “TM”

The corresponding microstructures at a mid-radius bar position as observed by light optical microscopy are shown in Figure 1. In order to inhibit the growth of austenite grains after severe deformation at elevated temperatures, the material should be subjected to rapid cooling thereafter. Thus, the changes in processing parameters between STD and TM steels do not only affect the prior austenite grain sizes but also the phase constituents. Although bainite is the dominant phase under both conditions, the conventionally hot rolled material exhibits more ferrite (due to slower cooling rates).

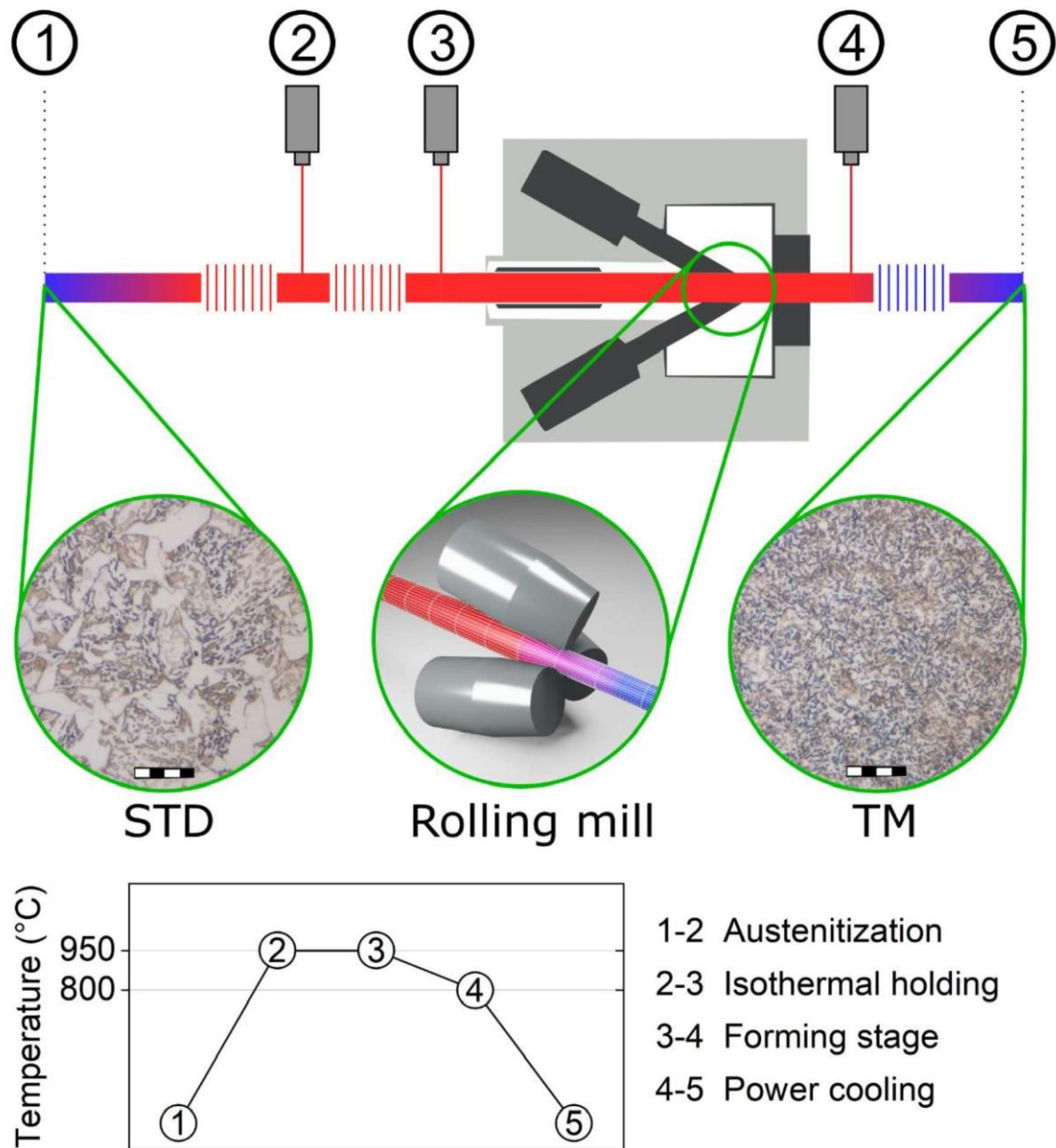


Figure 1: Schematic of the XTP® rolling line, depicting the micrographs of two investigated steels and a temperature profile during thermomechanical processing. The scale bars on the micrographs are 10  $\mu\text{m}$ .

The corresponding properties from static tensile testing are listed in Table 2.

Table 2 Static mechanical properties of STD and TM steels

Steel	Yield strength $R_{p0.2}$ (MPa)	Ultimate tensile strength $R_m$ (MPa)	Uniform elongation $A_g$ (%)	Reduction of cross section $Z$ (%)	Elongation at fracture $A_{5.65}$ (%)	Elongation at fracture $A_{manual}$ (%)
STD	533	838	9.0	58.0	19.2	19.1
TM	526	919	12.0	59.0	21.3	21.5

## 2.2 Experimental methods

### 2.2.1 Fatigue crack propagation

Load-controlled cyclic tests according to [25] were performed for both materials using compact tension (CT) samples in order to investigate the fatigue crack behavior. As a result, the fatigue crack growth rate was determined as a function of stress intensity factor  $\Delta K$  for a given R-ratio  $R = 0.1$ . The size of the cyclic plastic zone in the vicinity of the crack tip can be controlled by altering the stress intensity factor, which in turn is a function of the crack length and load. This provides an opportunity to analyze the microstructural changes (e.g. phase transformation, residual stresses and strains) near the crack tip, as well as to investigate the influence of those microstructural changes on crack propagation behavior and fatigue properties of material.

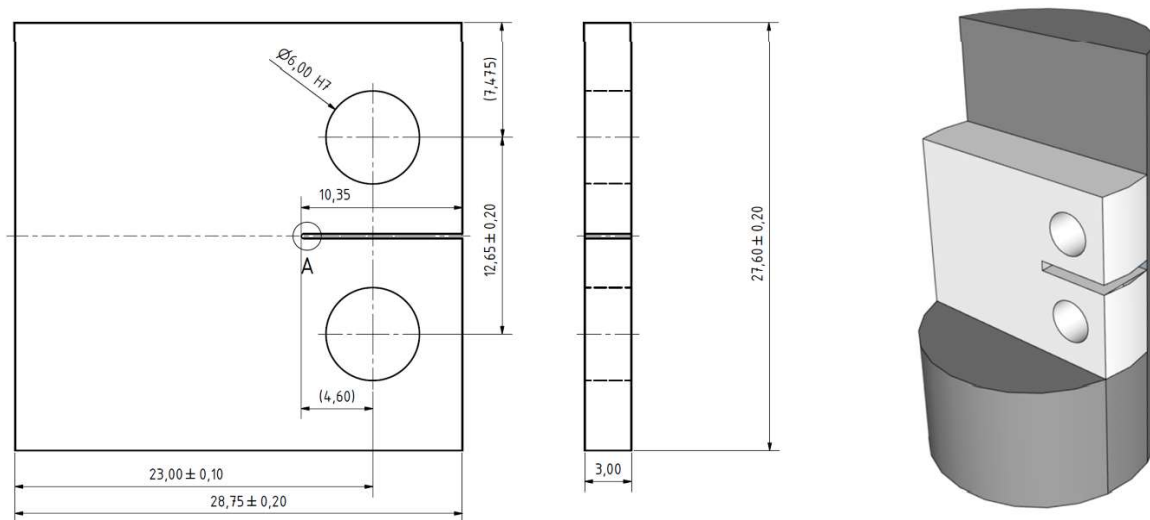


Figure 2: Sketch of the CT sample and its cutout orientation with respect to the steel bar. The dimensions are given in mm.

In comparison with the standard CT samples, the geometry of the samples used in this work had to be slightly modified. Due to fairly small diameters of the investigated steel bars ( $\varnothing 31$  mm and  $\varnothing 30$  mm for STD and TM, respectively), the dimensions of the specimens were proportionally scaled down, in order to ensure an adequate sampling (Figure 2). The CT samples were manufactured using electrical discharge machining in order to prevent the introduction of residual stresses from mechanical machining. The orientation of the notch and the consecutive crack is perpendicular to the axis of the steel bars. Finally, as recommended in [25], the samples were polished from both sides.

A high-frequency resonance test facility Rumul Mikrotron 654 with a maximal load capacity of  $\pm 5$  kN was used to investigate the fatigue crack propagation behavior. The testing frequency of resonance testing machines depends on the stiffness of the sample, as it is a part of an oscillating mass-spring system. An increase of crack length causes a decrease of the frequency, as the sample becomes more compliant. The testing frequency was in the range of 120-135 Hz. The crack length was measured from both sides of the sample using traveling microscopes and the average value was calculated.

In order to determine the fatigue crack growth rate as a function of  $\Delta K$  a combination of two procedures was used:  $\Delta K$ -decreasing with subsequent  $\Delta K$ -increasing. At the beginning of the test,  $\Delta K$  was gradually decreased in order to estimate a part of the Paris region and the threshold  $\Delta K_{th}$ . The latter one was established, as the crack growth rate  $da/dN \leq 10^8$  m/cycle was reached. After that,  $\Delta K$  was progressively increased for the determination of the Paris region for higher crack propagation rates. Finally, the fracture toughness  $K_{IC}$  was determined by quasistatically loading the CT samples with previously grown fatigue crack until failure.

Additionally, a number of crack growth tests were performed to initiate the fatigue crack for various investigations, including VSM, HEXRD, etc. They are summarized in Table 3.

Table 3: Summary of CT samples and subsequent investigations

Sample	Material	Type of crack growth test	Fatigue crack length $a$ , mm	Maximum stress intensity $\Delta K$ at the crack tip/ Range of stress intensity factor $\Delta K$ , MPa $m^{0.5}$	Subsequent investigations
CT-STD-1	STD	$\Delta K$ -decrease with subsequent $\Delta K$ increase / Fracture toughness	11.62	5.6-71.5	Fractography
CT-TM-1	TM	$\Delta K$ -decrease with subsequent $\Delta K$ increase/ Fracture toughness	11.8	7.2-69.1	Fractography
CT-STD-2	STD	$\Delta F$ -constant	13.6	34.8	Topography/VSM
CT-TM-2	TM	$\Delta F$ -constant	13.56	34.6	Topography/VSM
CT-STD-3	STD	$\Delta F$ -constant	12.6	35	HEXRD
CT-TM-3	TM	$\Delta F$ -constant	16	45	HEXRD

### 2.2.2 Topographic characterization

Topographic investigations of the CT sample surfaces along the fatigue crack were carried out using an optical profilometer Leica DCM8. An array of images of the sample surface was taken while operating the optical profilometer in confocal mode in order to acquire a sufficiently large area. The subsequent reconstruction and stitching of surface topography images was done automatically using the software Leica SCAN 5.4 . Post processing and further analysis of acquired topographical data was done using Leica Map 7.4.

### 2.2.3 Microstructure characterization

EBSM measurements were done on a Hitachi S4800 electron microscope using an electron energy of 20 keV and a 70° sample tilting. Samples were prepared by standard metallography techniques including grinding to P4000 followed by 3  $\mu m$  and 1  $\mu m$  diamond suspension polishing and final polishing using 50 nm silica colloidal suspension. Phase indexing was performed by including both face centered cubic (fcc) and body centered cubic (bcc) crystal structures. Phase maps and kernel average misorientation (KAM) maps were plotted. KAM maps reveal local lattice misorientation associated with strain gradients which can stem from defects



or other phases [26]. The SEM images of the fracture surfaces were taken with a FEI Nano-SEM230.

## 2.2.4 Vibrating sample magnetometry

Vibrating sample magnetometry (VSM) measurements were done on a physical property measurement system (PPMS) from Quantum Design. VSM measurements allow to obtain phase fractions of paramagnetic austenitic fcc phase and ferromagnetic bcc phase, assuming that cementite is absent in the investigated materials. This assumption has been validated by additional XRD measurements, which showed for all samples only the presence of these two crystal structures. The VSM measurements were done under two conditions. First, the phase fractions were determined in the undeformed state. Afterwards, the VSM measurements were done in the vicinity of a crack tip to determine the deformation induced phase transformation from austenite to martensite.

For all measurements cylindrical samples with weights in the range of 50-100 mg were cut out by using electrical discharge machining. Four different samples were taken from the material in unreformed state at four different positions as shown in Figure S1 of the supplementary file.

The saturation magnetization was measured by magnetizing samples to 40000 Oe which corresponds to 4 T. The saturation magnetization was obtained from the magnetization curves by fitting the measured data using equation:

$$M = M_s \left( 1 - \frac{a}{H} - \frac{b}{H^2} \right) \quad (1)$$

where  $M$  is the magnetization,  $M_s$  is the saturation magnetization,  $H$  is the applied magnetic field,  $a$  and  $b$  are fitting parameters [27]. The saturation magnetization of  $\alpha$ -Fe is  $M_s^{Fe} = 218$  emu/g. However, due to the presence of alloying elements, the steel 13MnSiCr7 contains only 95 wt% Fe. As a consequence, it is assumed that the saturation magnetization of the material consisting solely of ferromagnetic bcc phase is  $M_s^{bcc} = 0.95 M_s^{Fe} = 207$  emu/g. The fraction of residual austenite is then calculated according to

$$V_{RA} = 1 - \frac{M_s}{M_s^{bcc}} \quad (2)$$

## 2.2.5 High energy synchrotron X-ray diffraction

High energy synchrotron X-ray diffraction (HEXRD) was performed at the P07-HEMS beamline of PETRAIII, Deutsches-Elektronen-Synchrotron (DESY) [28], by using the experimental parameters summarized in Table 4. A previously tested CT sample was fixed in a stepping xyz stage as shown in Figure 3a. The region in the vicinity of the crack tip was scanned perpendicularly to the X-ray beam using a step size of 0.2 mm in  $z$  and 0.5 mm in  $x$  direction (Figure 3b). The

entire Debye-Scherrer rings (Figure 3c) were acquired in transmission mode from each point of the area indicated in Figure 3b. The acquired diffraction images were segmented into 10 deg slices perpendicular and parallel to the crack growth direction (red slices in Figure 3c). After azimuthal integration of the segments, the resulting diffraction information was quantitatively evaluated for phase fraction and change in lattice parameter by Rietveld refinement as implemented in the TOPAS software package.

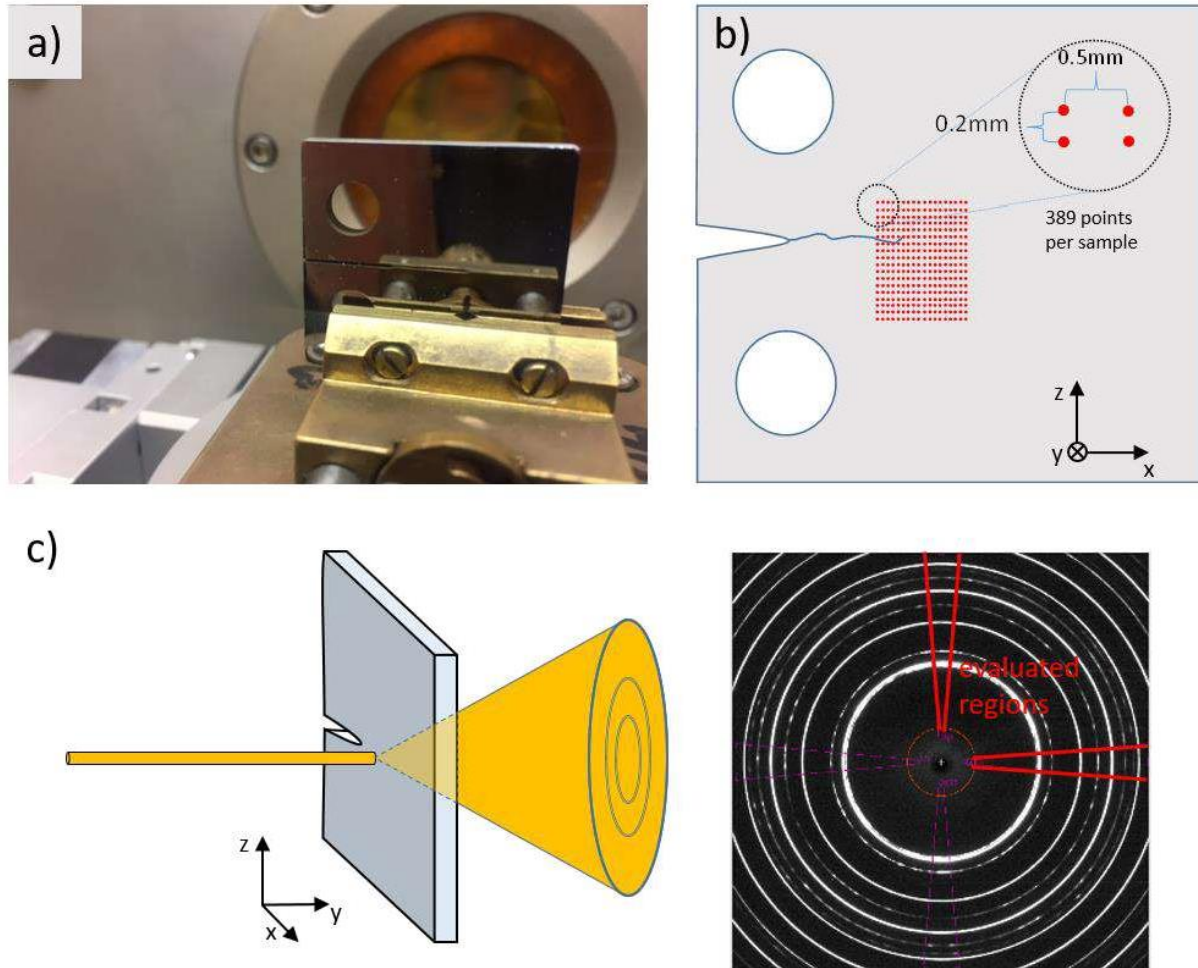


Figure 3: Employed HEXRD setup at P01-PETRAIII: a) sample setup on XYZ stage b) acquisition matrix covering an area of 5×7 mm (X×Z), c) orientation of the sample and segmentation of the Debye-Scherrer rings

Table 4: HEXRD experimental parameters.

Energy [keV]	Wavelength [Å]	Slit-aperture size [mm]	Step size [mm]	Sample-detector distance [mm]	Acquisition time [s]	Detector
100	0.124	0.2x0.2	0.2 in z 0.5 in x	1543.59	Sum of 5 images with an exposure time of 0.5s	Perkin Elmer XRD 1621 2048x2048px

## 3 Results

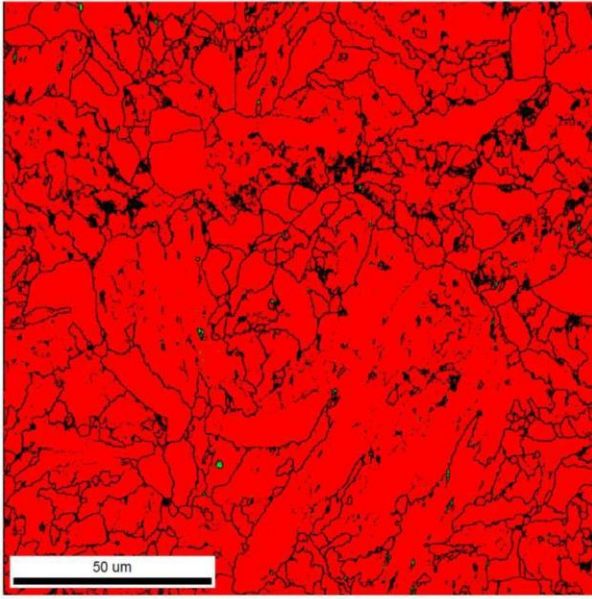
### 3.1 Electron back scattering diffraction (EBSD)

The EBSD mapping was performed to determine the amount of residual austenite. Samples for EBSD measurements were taken from the center of bars for both STD and TM materials. All data points with a confidence index smaller than 0.1 were removed. The EBSD phase maps of both STD and TM steels in Figure 4a and Figure 4c show nearly fully bcc crystal structures with very insignificant amount of confidently indexed fcc regions. In bainitic TRIP-assisted steels the residual austenite can appear in block and lamellar forms, both of which exhibit high degree of lattice distortion caused by interstitial C atoms. It is possible, that at least part of the unindexed data points on the phase maps may be regarded as blocks of residual austenite. This indicates the limitation of the EBSD method, as both STD and TM steels are expected (and will be proven later) to contain bigger fraction of residual austenite.

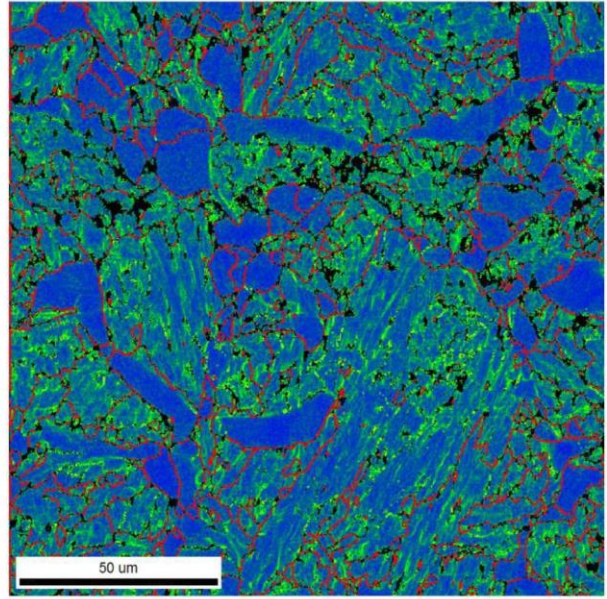
The KAM maps were plotted to further examine the materials' microstructure (see Figure 4b and Figure 4d). Grains that encompass insignificant misorientation of less than  $1^\circ$  (homogeneously blue regions) are ferrite. The volume differences between bainite and residual austenite cause localization of orientation gradients near phase boundaries [29]. Thus, the regions mapped in green are most probably the combination of bainitic ferrite and lamellar residual austenite. Due to the morphology and small size, the grains of the latter were not clearly identified as fcc crystals.



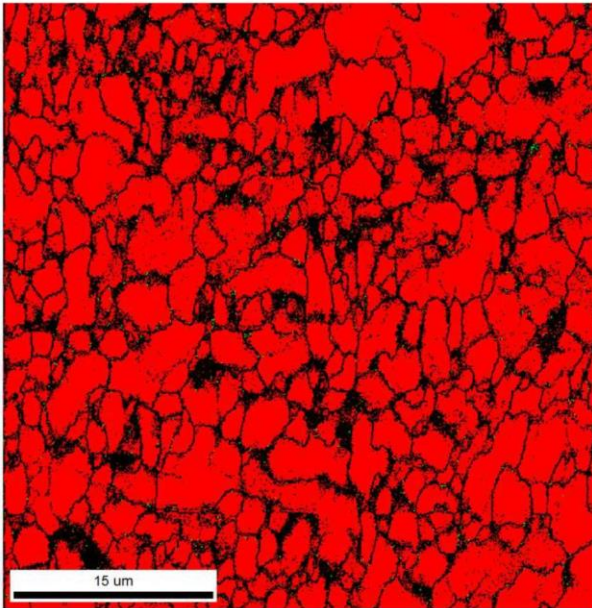
a) STD phase map



b) STD KAM



c) TM phase map



d) TM KAM

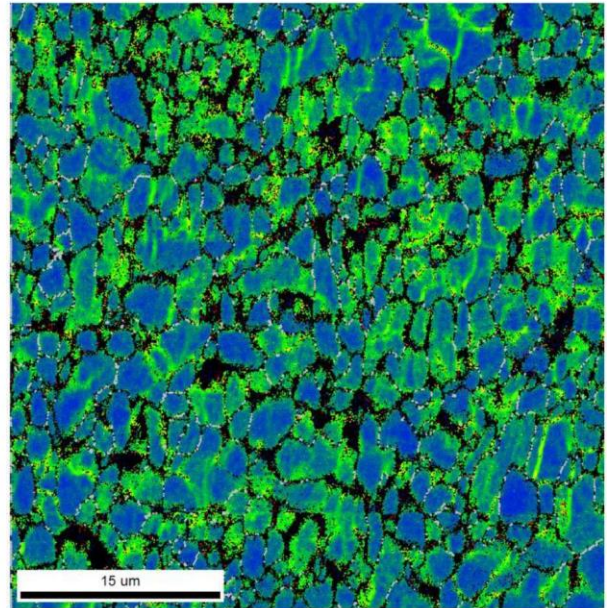


Figure 4: a) and c) EBSD phase maps of STD and TM steels. Red and green colors indicate bcc and fcc crystal structures respectively. b) and d) kernel average misorientation. Grain boundaries are shown in red. Note the difference in magnification between a), b) and c), d) reflecting the smaller grain size of TM steel.

### 3.2 Fatigue crack propagation behavior

The results of the fatigue crack growth rate as a function of stress intensity factor  $\Delta K$  of two CT samples, namely CT-STD-1 and CT-TM-1, are presented in Figure 5. The Paris region represents a stable crack growth condition. The experimental results indicate a slower crack propagation

in TM steel compared to STD. Furthermore, the threshold value of the stress intensity factor  $\Delta K_{th}$  is higher for TM steel. This means that under the same loading conditions the TM steel will tolerate longer cracks without further growth than STD (or otherwise can withstand higher loading, provided the same crack length in both materials).

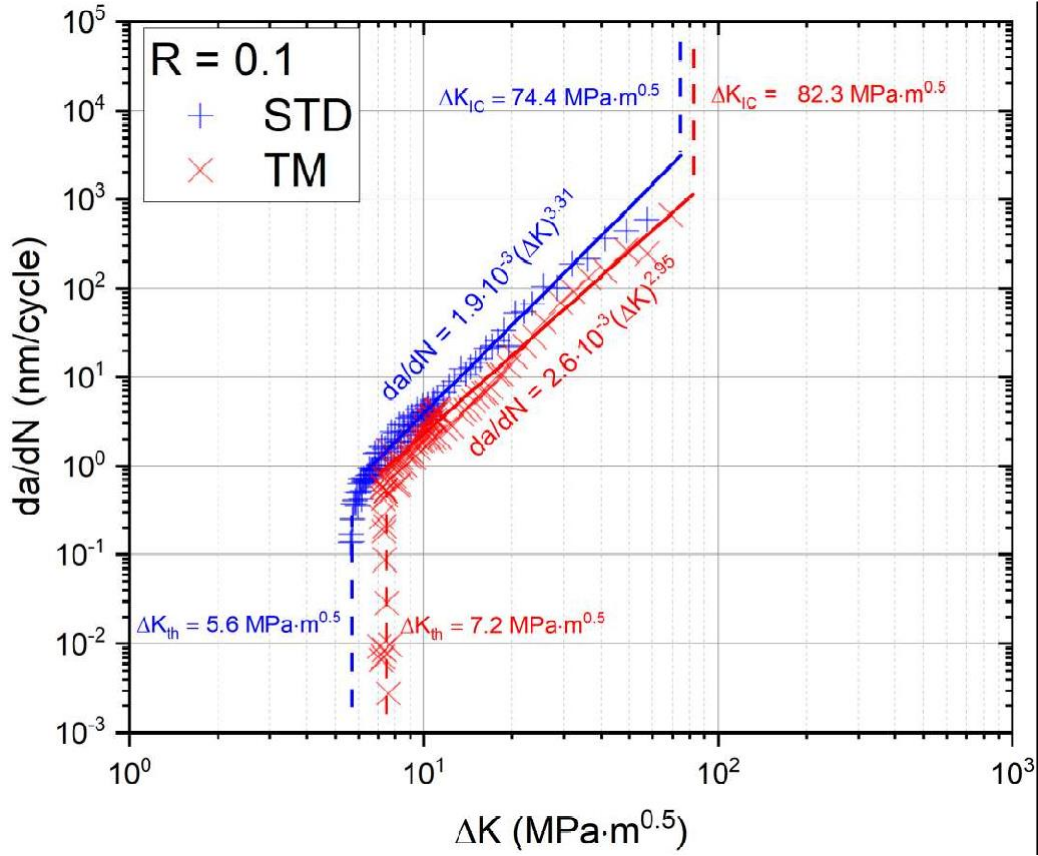


Figure 5: Fatigue crack growth rate as a function of  $\Delta K$  for STD and TM steel

### 3.3 Topography of the surface along the fatigue crack

Due to the substantial difference in grain size between STD and TM, it was interesting to compare the size of the cyclic plastic zones near the fatigue crack tip. For this purpose, two CT-samples (CT-STD-2 and CT-TM-2) were produced with similar crack lengths and stress intensity factors using the same constant loading amplitude. Thus, as the crack propagated through the sample, the stress intensity factor at its tip increased. After that, the samples were investigated using an optical profilometer. The comparison of surface topography along the fatigue crack as well as the overview images of the cracks are shown for STD and TM steels in Figure 6.



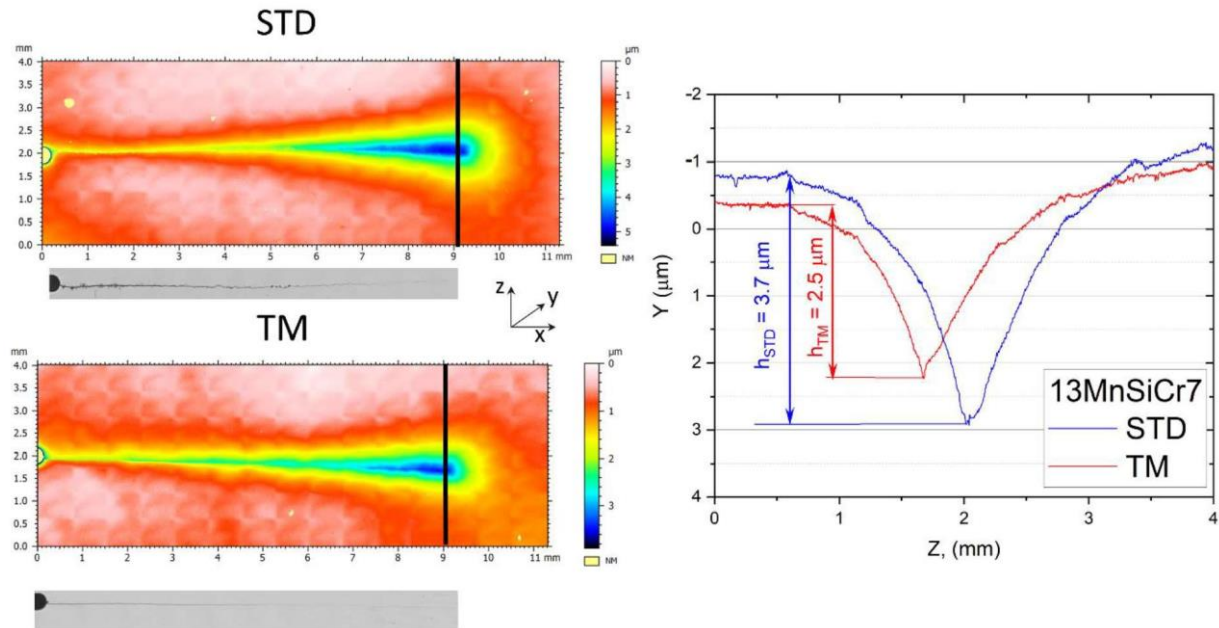


Figure 6 Topography of the surface along the fatigue crack of CT-samples of STD and TM steels. Extracted profiles (associated lines indicated on the X-Z maps), and macroscopic images of the fatigue crack.

As the fatigue crack propagates through the material, it causes extensive plastic deformation creating the cyclic plastic zone at its tip. The size of this region is proportional to the magnitude of the stress intensity factor  $\Delta K$ . Consequently, the progressively increasing stress intensity factor  $\Delta K$  in the CT-samples CT-STD-2 and CT-TM-2 caused an expansion of the plastic zone. This is manifested as an enlargement of the valley/groove along the path of fatigue crack (Figure 6). After extracting the surface profiles perpendicular to the crack path at the crack tip it is obvious that the plastic deformation in the sample CT-STD-2 is more pronounced than in CT-TM-2, as this valley is both deeper and wider. It is also worth noting that the fatigue crack path in the STD sample is more jagged than in the TM sample.

### 3.4 Vibrating sample magnetometry

The undeformed STD steel has a homogeneously distributed fcc phase varying between 7.5 and 8.5 vol% (average 8 vol %). For the undeformed TM steel the fcc phase is homogeneously distributed in the inside of the bar with a phase fraction between 10 and 11 vol% (average 10.5 vol%), while at the peripheral layers of the bar the fcc phase content drops to only 1 vol% (see Figure S3 in the supplementary file).

Cylindrical (bulk) VSM samples were taken in perpendicular direction from the crack tip. Figure S2 in the supplementary document shows the location of the measured samples in the vicinity of the crack tip. For the TM steel, a total of five specimens at 0 mm, 1 mm and 2 mm on both

sides from the crack were used, while for the STD steel only three cylindrical samples were prepared (at 0 mm, 1 mm and 2 mm distance on one side from the crack).

The TM samples show an increase of the fcc content with increasing distance from the crack tip, which is an indicator of the phase transformation. At the crack tip, the amount of residual austenite is around 6 vol% (Figure 7), which is lower when compared with the sample in the undeformed state. However, this value might be even lower than 6 vol% directly at the crack tip itself, considering the relatively large volume of the VSM samples. The diameter of the VSM samples is  $\sim 0.5$  mm, which is on the order of magnitude of the plastic zone near the crack tip. A similar trend, although with somewhat lower values, is observed in the STD material, for which a value of 5 vol% residual austenite was measured near the crack tip (Figure 7). As in the case of the TM sample, this drop is likely due to the fcc to bcc transformation.

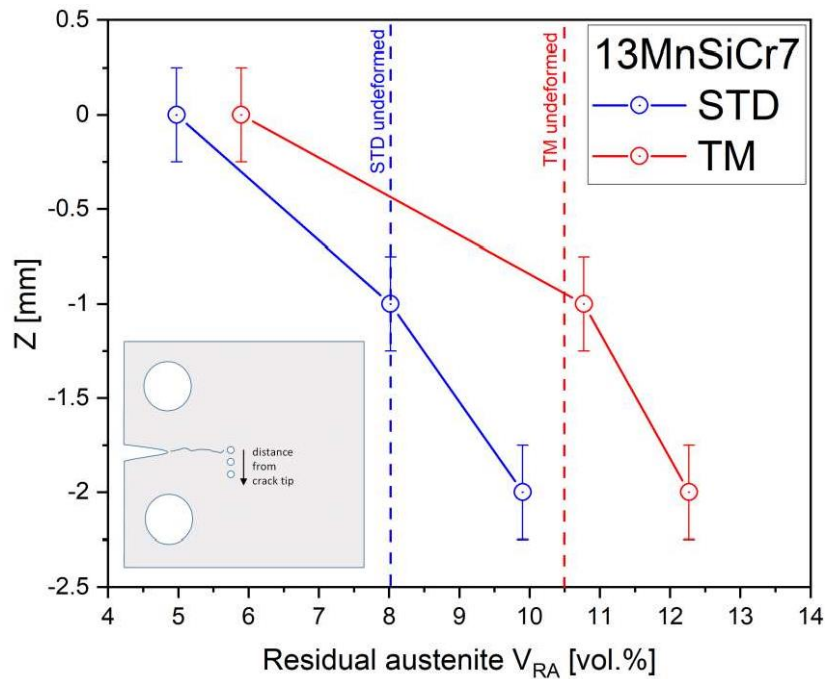


Figure 7: Determination of the residual austenite at the crack tip of the samples CT-STD-2 and CT-TM-2 using VSM. The average residual austenite content for the undeformed materials is shown with vertical dashed lines. The scale bars correspond to the diameter of cylindrical specimens for VSM (0.5 mm)

### 3.5 High-energy synchrotron X-ray diffraction

HEXRD experiments were utilized to get insight on quantitative bulk phase fraction and residual strains after interrupted fatigue crack growth experiments of the CT samples CT-STD-3 and CT-TM-3. Figure 8a shows the color-coded maps of the selected region of the fcc phase fraction distribution obtained by the HEXRD. The very fine-grained structure and the equally small distributed fcc phase lead to accurate phase identification during Rietveld refinement. Due to the small grains and homogenous distribution of the fcc phase, an average residual austenite

content in TM material was determined to be ~11 vol.% (Figure 8b), which corresponds well with the VSM measurements. The presented phase fractions were determined by Rietvelt refinement fitting the bcc and fcc phase simultaneously. As shown in Figure 8c, along the indicated crack path (black line) a clear change in microstructure and an increased amount bcc phase is observed, indicating the occurred phase change. A minimum amount of the residual austenite of ~1.8 vol.% is found right in front of the crack tip.

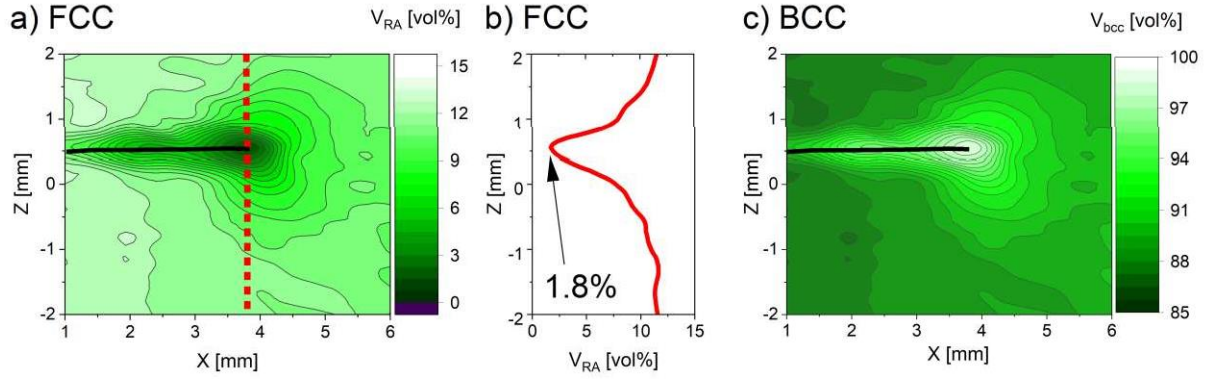


Figure 8: a) fcc phase fraction in TM steel in the vicinity of the crack tip, b) average fcc content integrated in the marked area, c) phase fraction in TM steel.

Figure 9 shows the average lattice strains for the fcc and bcc phases perpendicular ( $\epsilon_{zz}$ ) and parallel ( $\epsilon_{xx}$ ) to the crack propagation direction. The lattice strain was calculated using the relative variation of the refined lattice parameter ( $a$ ) across the sample in the usual way, i.e.

$$\epsilon = \frac{a - a_0}{a_0} \quad (3)$$

This approach has the advantage that, by including many peaks in the refinement, the measured strains are likely to be representative of the macroscopic response, free from significant elastic or plastic anisotropy effects. The unstrained lattice parameter ( $a_0$ ) was obtained from the averaged far-field measurement in the unloaded state.

The strain fields indicate pronounced compressive strains at the crack tip in both x- and z- directions, with more pronounced compressive strain field in the fcc phase.



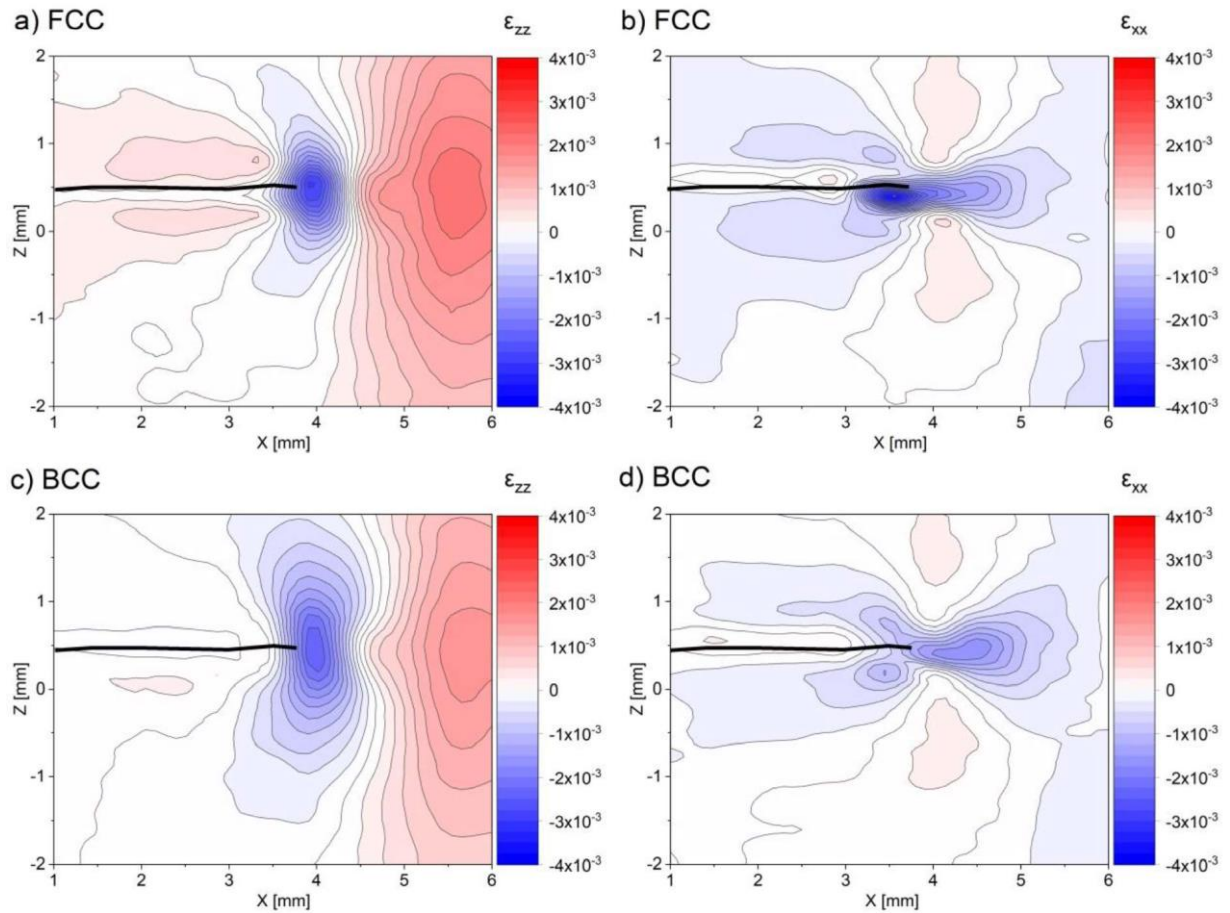


Figure 9: Strain in fcc phase along the mapped area for the TM steel for the directions a) perpendicular to the crack propagation  $\epsilon_{zz}$  and b) parallel to the crack propagation  $\epsilon_{xx}$ . The corresponding strain fields in the bcc phase are shown in c) and d), respectively.

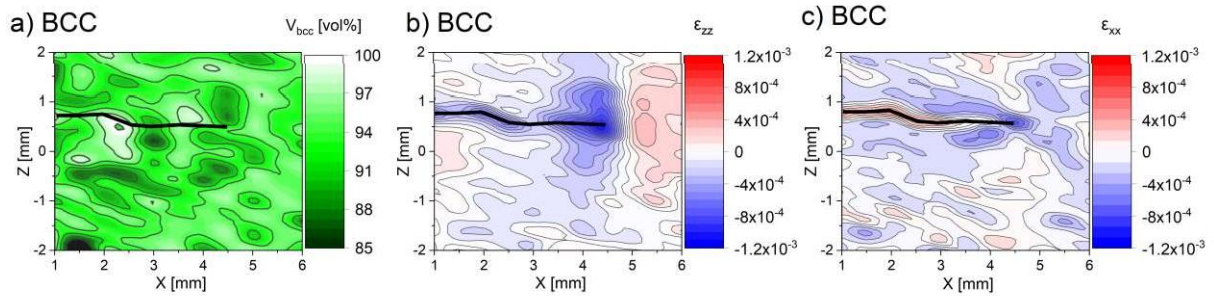


Figure 10: a) bcc phase fraction in STD steel in the vicinity of the crack tip. Strain field in b) perpendicular to the crack propagation  $\epsilon_{zz}$  and c) parallel to the crack propagation in  $\epsilon_{xx}$  direction.

For the STD steel with a much larger grain size as evident from previously shown EBSD images (see Figure 4), the equivalent phase- and strain maps are shown in Figure 10. Islands of fcc rich and poor regions are distributed equidistantly in the observed microstructure, making it challenging to directly identify phase transformation. Due to the larger grains and the coarser distribution of fcc islands in the STD samples, it is more difficult to clearly recognize a crack path in the phase map. However, the residual strain fields in x and z direction are still clearly visible.

A clear compressive strain field in front of a more jagged crack path is observed, presenting a maximum intensity right in front of the crack tip.

### 3.6 Fractography

For a better understanding of the fatigue crack propagation behavior, fractographic investigations of the CT sample CT-STD-1 were carried out in the SEM. The fractograms presented here were taken in the zones of the cracks surface, where the stress intensity factor was in the range 32-36 MPa  $m^{0.5}$ . On a somewhat larger scale, the fracture surface of CT-STD-1 seems to be fairly rough (Figure 11 a). The detailed investigation revealed quite pronounced striation lines (Figure 11 b), which indicates stable crack growth. Over a length of 4  $\mu m$  around 20-24 lines were counted, which would result in a crack propagation rate in the range of 160-200 nm/cycle. This corresponds fairly well to the actually measured crack propagation rates in that region. Furthermore, multiple secondary cracks perpendicular to the main fatigue crack were observed, which indicates crack branching.

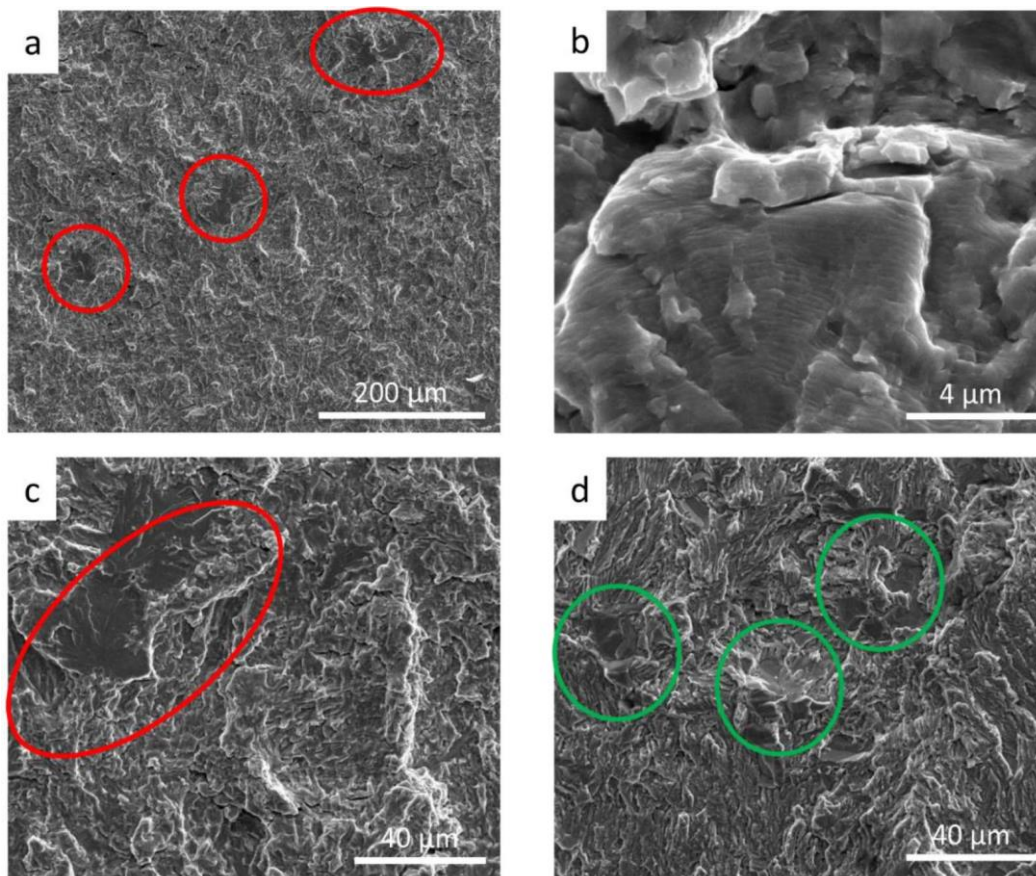


Figure 11: Fracture surface of sample CT-STD-1. Red ellipses indicate brittle cleavage fracture, while green ellipses indicate intergranular fracture. Crack propagation direction is bottom-top.

Further investigations of the fracture surface revealed additional features. Multiple regions of brittle cleavage fracture can be observed. These are indicated in Figure 11a and Figure 11c with

red ellipses, with no visible striation lines on them. It is possible that these cleavage fracture zones are ferrite grains, considering their size (approx. 40-80  $\mu\text{m}$ ) and referring to the results of EBSD phase maps (Figure 4). Moreover, it is well known that cleavage fracture occurs in ferrite on  $\{100\}$  planes [30,31]. As a result, when the fatigue crack reaches the ferrite grain with a preferable orientation, it propagates significantly faster due to the brittle fracture. It can also be noticed that occasionally the fatigue crack propagated along the grain boundaries, resulting in intergranular fracture (see Figure 11d, green ellipses), which can be caused by insufficient cohesion between grains. These regions with intergranular fracture also accelerated the fatigue crack propagation. Thus, the combination of these factors probably contributed to inferior fatigue behavior of STD material in comparison with TM.

The fracture surface of CT-TM-1 sample (Figure 12) is considerably smoother and more homogeneous in comparison with CT-STD-1 sample. This is consistent with the fact that the fatigue crack in TM material is considerably more linear than in STD (see Figure 6). No features with cleavage or intergranular type fracture were observed. It must be pointed out that the overall prior austenite grain boundary surface is increased by a factor of 25, if the grain size is reduced to 1/5. Consequently, the average grain boundary concentration of harmful segregated atoms (e.g. phosphorus) lowering grain boundary cohesion than is reduced to 1/25 (4%). This explains why grain boundary decohesion is more likely to occur if the prior austenite grain size is larger. Similar to STD steel, striation lines were detected as well (Figure 12). However, they are significantly less pronounced. From these lines a crack propagation rates of 70-80 nm/cycle was estimated, which again, matches with values reported in Figure 5.

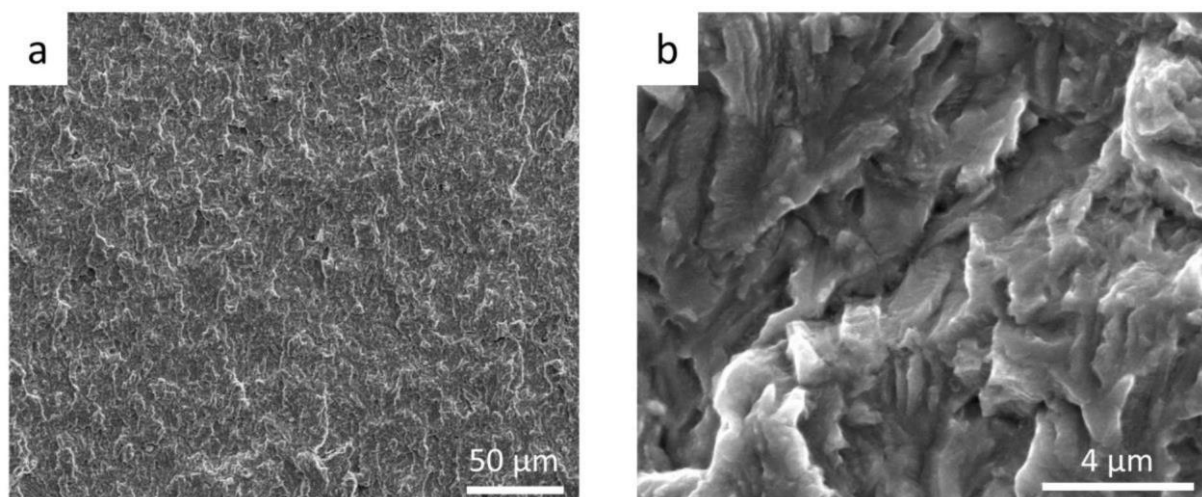


Figure 12: Fracture surface of sample CT-TM-1. Crack propagation direction is bottom-top.

## 4 Discussion

### 4.1 Influence of grain size on TRIP effect and fatigue crack growth behavior

The results of the fatigue crack growth tests (Figure 5) indicate an improved performance of TM in comparison with STD material. However, it is well known that despite significant improvement in endurance strength, grain refinement can deteriorate the resistance to fatigue crack propagation. Previous studies have proven this for metallic materials with both fcc (e.g. aluminum alloys [32,33] or copper [34]), as well as with bcc (e.g. IF steel [35], or low carbon steel [36]) microstructures. The effect is mostly attributed to the small grain size, which hinders the mobility of dislocations and their ability to cross grain boundaries [37]. Thus, the observed improvement in fatigue crack resistance in this work cannot be explained by grain refinement and might be attributed to the TRIP effect.

Plastic deformation of steels with residual austenite can cause its transformation into martensite [38]. Numerous investigations have shown that the TRIP effect can be used to improve the fatigue properties of bainitic TRIP steels. A significant enhancement of endurance strength, especially upon overloads, was reported in [39–44]. The associated increase in performance was explained by closure of the fatigue crack tip by compressive stresses due to the phase transformation. The stability of the residual austenite is primarily determined by its chemical composition (particularly carbon content) and grain size [45]. Thus, the finer grains of residual austenite in TM steel are inherently more stable than coarser grains in STD. On the other hand, when the residual austenite grains become too stable, they might not exhibit martensitic transformation [46]. Hence, three main questions arose at the beginning of this investigation: (a) whether the martensitic transformation in TM steel takes place, (b) in how far the TRIP effect contributes to improvement in crack propagation resistance, and (c) how the increased stability of refined residual austenite influences the crack propagation.

In the analytical approach for the calculation of a radius of a plastic zone [47] it is assumed that this radius is a function of the stress intensity factor, yield strength of the material, as well as the stress state (i.e. plane stress/strain). Considering that these parameters are identical or comparable in the CT-STD-1 and CT-TM-1 samples, it is expected that the radii of the plastic zones should be also similar. However, as mentioned above (see Figure 6), the plastic deformation near the crack tip in STD steel is more pronounced than in TM. The observed discrepancy can be associated with the considerable grain refinement in TM steel. The amount of grains per unit volume of the material increases as the grain size decreases. Thus, the plastic zone near the crack tip in the TM sample interacts with a larger number of grains, and the crack has to pass through more grain boundaries. Furthermore, the microstructure in the TM samples is significantly more homogeneous, which leads to a more uniform distribution of residual stresses near the crack tip.

In order to investigate the microstructure and phase changes in the STD and TM steels, it is important to select appropriate characterization methods. In other studies on TRIP steels, mainly EBSD measurements were used for this purpose [3,48,49]. However, it is obvious from Figure 4 that it is hardly possible to resolve the residual austenite in both STD and TM steels by EBSD in the present work. Carbon is the main austenite stabilizing element in the investigated steels. Its concentration in the fcc phase is significantly higher (~1.2 wt%) than in the rest of the microstructure, which causes considerable distortion of the austenite lattice. It is speculated that this strain related distortion of the fcc austenitic phase results in a distortion of the backscattered diffraction patterns, hence, the simulated Kikuchi bands mismatch, or have a low confidence index, and are therefore unidentified and are colored in black in the EBSD map. The elastic strain can be confirmed by the KAM maps. Additionally, EBSD allows only the investigation of the surface layer of the material.

The amount of residual austenite in the investigated steels could be successfully estimated by VSM. For both the STD and TM samples a significant decrease of the amount of austenite by approx. 5 vol% in comparison with the undeformed state clearly indicate the phase transformation near the fatigue crack tip. However, the results of the VSM measurements are rather qualitative than quantitative, due to the rather large sample size for VSM and the limitations with respect to the precision of sample extraction.

HEXRD allowed obtaining high-resolution phase and lattice strain maps of both STD and TM steel. This provided the possibility to quantitatively characterize the effect of the propagating fatigue crack on the phase transformation. For the TM steel, a minimum amount of less than 2 vol% of residual austenite was measured directly at the crack tip, which corroborates the results from the VSM measurements. The austenite-to-martensite phase transformation is more difficult to observe in the STD sample, presumably due to the significantly coarser microstructure. Pronounced compressive strains were measured in the vicinity of the crack tip for both the STD and TM samples. The high stress concentration near a crack tip can trigger the transformation process, hence small regions of fcc can transform into bcc. This transformation, and the associated dilatation can cause the crack to close, and thus the overall stress concentration near the crack tip decreases enhancing the fracture toughness, which increases the resistance to fatigue crack growth.

#### 4.2 Contribution of martensitic transformation to fracture toughness

Chen et al. proposed an approach for estimating the effect of the martensitic transformation on fracture toughness of TRIP steel [3]. For this purpose, the following equation was used

$$(\Delta K_c)_{A \rightarrow M} = \sqrt{\Delta R_{A \rightarrow M} \cdot E} = \sqrt{\left(\sigma_m \cdot \frac{\varepsilon_{IS}}{\sqrt{3}}\right) \cdot 2r_p \cdot \bar{V}_M \cdot E} \quad (4)$$

where  $\sigma_m$  is the stress required to initiate the phase transformation (it was assumed to be equal to the yield stress of the corresponding steel in this calculation and given in Table 2),  $\epsilon_{IS}$  is the invariant strain associated with the transformation ( $\epsilon_{IS} = 0.2$ ),  $r_p$  is the radius of the monotonic plastic zone,  $\bar{V}_M$  the average volume fraction of martensite, that was formed inside the monotonic plastic zone during fracture process, and  $E$  is the modulus of elasticity. For the calculations according to this equation, firstly we need to determine two parameters, namely  $r_p$  and  $\bar{V}_M$ .

The profiles of the volume fractions of residual austenite in STD and TM steels are shown in Figure 13 and were extracted from the HEXRD data presented in Figure 8 and Figure 10, respectively. Due to pronounced plastic deformation in the plastic zone, the martensitic transformation takes place. Consequently, a decreased austenite content locates near the crack tip. As the distance from the crack tip increases, the content of residual austenite increases too, and reaches the average values of the undeformed STD and TM samples at roughly 1.1 mm and 1.9 mm, respectively. These values correspond reasonably well to the radius of the monotonic plastic zone for plane strain conditions, which can be approximately estimated according to the equation

$$r_p = \frac{1}{3\pi} \left( \frac{K_{max}}{\sigma_y} \right)^2 \quad (5)$$

For the quantitative determination of the amount of RA, the curve fitting of the data was performed using the following function

$$V_{RA} = a - b \cdot c^p \quad (6)$$

The estimated functions are given in Figure 13.

The average volume fraction of martensite  $\bar{V}_M$  was determined as the difference between the content of residual austenite in the undeformed material and the average amount of the residual austenite in the monotonic plastic zone. This resulted in values for  $\bar{V}_M$  of 1.9 and 2.9 vol% in the STD and TM samples, respectively.

The fracture toughness of STD and TM samples were experimentally estimated to be 74.4 MPa m<sup>0.5</sup> and 82.3 MPa m<sup>0.5</sup>, respectively, (see Figure 5). After performing the calculations according to equation (4), the contribution of phase transformation to the fracture toughness was estimated to be 31.9 MPa m<sup>0.5</sup> and 43.8 MPa m<sup>0.5</sup>, i.e. 42% and 53%, correspondingly. Thus, it can be concluded that the TRIP effect in TM steel contributes significantly more to the improved fatigue crack resistance. Taking into account the residual austenite contents in the bulk material (8 vol% vs. 10.5 vol%), the increases in fracture toughness are 4.0 MPa m<sup>0.5</sup> (STD) and 4.2 MPa m<sup>0.5</sup> (TM) per vol% of residual austenite. At the same time, the TM steel has larger amount of residual austenite, as well as higher volume fraction of transformed martensite, compared to STD steel. Subsequently, we can assess the specific increase of fracture toughness per vol.% of



transformation induced martensite, which results to 16.8 MPa m<sup>0.5</sup> per vol% for STD and 15.1 MPa m<sup>0.5</sup> per vol% for TM. This results indicates that the retained austenite in TM is more stable, although the difference is small.

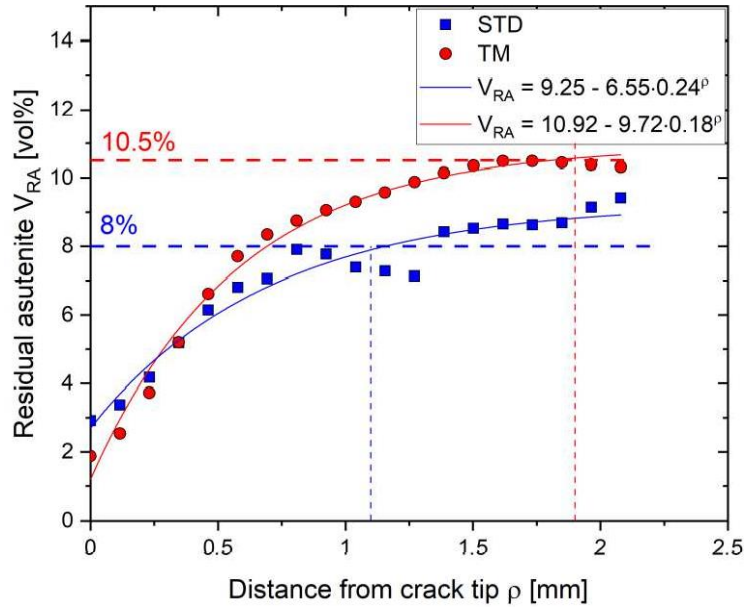


Figure 13: Volume content of residual austenite as a function of the distance from the crack tip. Thick dash lines indicate average content of residual austenite in steels.

## 5 Conclusions

In this study, two low-alloyed bainitic TRIP-assisted steels with identical chemical compositions but with different processing methods have been investigated: the reference (STD) steel was conventionally rolled, whereas new micro-bainitic TRIP steel (TM) underwent additional thermomechanical treatment (was re-rolled) using a novel XTP® technology. Consequently, the investigated steels had significant differences in microstructure (in terms of residual austenite content, as well as grain size), which allowed to estimate the effects of grain refinement on their crack propagation properties. The main results can be summarized as follows:

1. Lowering the hot rolling temperature from 1100°C to 800°C by applying the XTP® technology, the retained austenite content of new micro-bainitic TRIP steel could be increased by ~30%.
2. After applying the thermomechanical treatment to the STD steel, the TM steel showed an improvement of the fatigue crack propagation properties (i.e. threshold  $K_{th}$ , crack propagation rate, and fracture toughness  $K_{IC}$ ).
3. While EBSD proved to have limitations to quantify the amount of the highly distorted residual austenite, the austenite volume fraction and the amount of martensite in the vicinity of the fatigue crack could be successfully estimated by VSM and HEXRD.
4. The estimated total contribution of the TRIP effect to the fracture toughness is higher in TM steel than in STD steel. This can be explained by higher residual austenite content (10.5 vol% for TM and 8 vol% for STD). The fracture toughness rises by 4 MPa m<sup>0.5</sup> for each 1 vol% increase in residual austenite.
5. By applying the additional thermomechanical treatment the occurrence of cleavage fracture could be reduced. This might be explained with a reduced grain boundary concentration of segregated and embrittling atoms.

## Data availability

The data will be made available upon reasonable request

## CRediT authorship contribution statement

I. Burda: Conceptualization, Methodology, Data curation, Visualization, Investigation, Formal analysis, Writing – original draft

K. Zweigacker: Methodology, Investigation, Data curation, Visualization, Writing – review & editing

A. Arabi-Hashemi: Methodology, Investigation, Data curation, Writing – review & editing



P. Barriobero Vila: Methodology, Writing – review & editing  
A. Stutz: Methodology, Investigation, Writing – review & editing  
R. Koller: Project administration, Funding acquisition, Writing – review & editing  
H. Roelofs: Resources, Project administration, Writing – review & editing  
L. Oberli: Methodology, Writing – review & editing  
M. Lembke: Methodology, Writing – review & editing  
C. Affolter: Project administration, Writing – review & editing  
C. Leinenbach: Project administration, Funding acquisition, Resources, Writing – original draft

## **Declaration of competing interest**

The authors declare that they have no known competing financial interests or personal relationships that could have appeared to influence the work reported in this paper

## **Acknowledgement**

The work was supported by the Swiss Innovation Agency (project number 27126.1 PFIW-IW), which is gratefully acknowledged.

## References

- [1] E. Girault, A. Mertens, P. Jacques, Y. Houbaert, B. Verlinden, J. Van Humbeeck, Comparison of the effects of silicon and aluminium on the tensile behaviour of multiphase TRIP-assisted steels, *Scr. Mater.* 44 (2001) 885–892. [https://doi.org/10.1016/S1359-6462\(00\)00697-7](https://doi.org/10.1016/S1359-6462(00)00697-7).
- [2] B. Yan, D. Urban, CHARACTERIZATION OF FATIGUE AND CRASH PERFORMANCE OF NEW GENERATION HIGH STRENGTH STEELS FOR AUTOMOTIVE APPLICATIONS, AISI-DOE Technol. Roadmap Program Rep. (2003) 97.
- [3] X. Cheng, R. Petrov, L. Zhao, M. Janssen, Fatigue crack growth in TRIP steel under positive R-ratios, *Eng. Fract. Mech.* 75 (2008) 739–749. <https://doi.org/10.1016/j.engfrac-mech.2007.01.019>.
- [4] K. Sugimoto, D. Fiji, N. Yoshikawa, Fatigue strength of newly developed high-strength low alloy TRIP-aided steels with good hardenability, *Procedia Eng.* 2 (2010) 359–362. <https://doi.org/10.1016/j.proeng.2010.03.040>.
- [5] T. Iwamoto, T. Tsuta, Computational simulation of the dependence of the austenitic grain size on the deformation behavior of TRIP steels, *Int. J. Plast.* 16 (2000) 791–804. [https://doi.org/10.1016/S0749-6419\(99\)00079-0](https://doi.org/10.1016/S0749-6419(99)00079-0).
- [6] H. Mughrabi, H.W. Höppel, Cyclic Deformation and Fatigue Properties of Ultrafine Grain Size Materials: Current Status and Some Criteria for Improvement of the Fatigue Resistance, *MRS Online Proc. Libr. OPL.* 634 (2000). <https://doi.org/10.1557/PROC-634-B2.1.1>.
- [7] T. Niendorf, Ermüdungseigenschaften ultrafeinkörniger kubisch raumzentrierter Werkstoffe: Einfluss der Mikrostruktur, 2010. <http://digital.ub.uni-paderborn.de/hsmig/1764> (accessed May 5, 2021).
- [8] T. Niendorf, H.J. Maier, D. Canadinc, I. Karaman, On the Cyclic Stability and Fatigue Performance of Ultrafine-Grained Interstitial-Free Steel under Mean Stress, *Key Eng. Mater.* 378–379 (2008) 39–52. <https://doi.org/10.4028/www.scientific.net/KEM.378-379.39>.
- [9] T. Niendorf, D. Canadinc, H.J. Maier, I. Karaman, S.G. Sutter, On the fatigue behavior of ultrafine-grained interstitial-free steel, *Int. J. Mater. Res.* 97 (2006) 1328–1336. <https://doi.org/10.3139/146.101377>.
- [10] T. SAWAI, S. MATSUOKA, K. Tsuzaki, Low-and High-cycle Fatigue Properties of Ultrafine-grained Low Carbon Steels, *Tetsu--HaganeJournal Iron Steel Inst. Jpn.* 89 (2003) 726–733. [https://doi.org/10.2355/tetsutohagane1955.89.6\\_726](https://doi.org/10.2355/tetsutohagane1955.89.6_726).
- [11] M.D. Chapetti, H. Miyata, T. Tagawa, T. Miyata, M. Fujioka, Fatigue strength of ultra-fine grained steels, *Mater. Sci. Eng. A.* 381 (2004) 331–336. <https://doi.org/10.1016/j.msea.2004.04.055>.
- [12] D. Geist, C. Rentenberger, H.P. Karnthaler, Extreme structural inhomogeneities in high-pressure torsion samples along the axial direction, *Acta Mater.* 59 (2011) 4578–4586. <https://doi.org/10.1016/j.actamat.2011.04.003>.
- [13] Y. Cao, M. Kawasaki, Y.B. Wang, S.N. Alhajeri, X.Z. Liao, W.L. Zheng, S.P. Ringer, Y.T. Zhu, T.G. Langdon, Unusual macroscopic shearing patterns observed in metals processed by high-pressure torsion, *J. Mater. Sci.* 45 (2010) 4545–4553. <https://doi.org/10.1007/s10853-010-4485-5>.

- [14] P.R. Cetlin, M.T.P. Aguilar, R.B. Figueiredo, T.G. Langdon, Avoiding cracks and inhomogeneities in billets processed by ECAP, *J. Mater. Sci.* 45 (2010) 4561–4570. <https://doi.org/10.1007/s10853-010-4384-9>.
- [15] Y. Cao, Y.B. Wang, S.N. Alhajeri, X.Z. Liao, W.L. Zheng, S.P. Ringer, T.G. Langdon, Y.T. Zhu, A visualization of shear strain in processing by high-pressure torsion, *J. Mater. Sci.* 45 (2010) 765–770. <https://doi.org/10.1007/s10853-009-3998-2>.
- [16] S. Torizuka, M. Kuntz, Y. Furuya, M. Bacher-Hoechst, Effect of Tensile Strength and Microstructure on Notch-fatigue Properties of Ultrafine-grained Steels, *ISIJ Int.* 52 (2012) 910–914. <https://doi.org/10.2355/isijinternational.52.910>.
- [17] Y. Furuya, S. Matsuoka, S. Shimakura, T. Hanamura, S. Torizuka, Fatigue Strength of Ultrafine Ferrite-Cementite Steels and Effects of Strengthening Mechanisms, *Metall. Mater. Trans. A* 38 (2007) 2984–2991. <https://doi.org/10.1007/s11661-007-9355-7>.
- [18] Y. Furuya, S. Matsuoka, S. Shimakura, T. Hanamura, S. Torizuka, Effects of carbon and phosphorus addition on the fatigue properties of ultrafine-grained steels, *Scr. Mater.* 52 (2005) 1163–1167. <https://doi.org/10.1016/j.scriptamat.2005.01.035>.
- [19] C. Ruffing, Schwingfestigkeit und Mikrostruktur von ultrafeinkörnigem C45, 2015. <https://kluedo.ub.uni-kl.de/frontdoor/index/index/year/2015/docId/4038> (accessed May 5, 2021).
- [20] R. Rozmus, R. Kuziak, L. Oberli, H. Roelofs, New fine grained temper-resistant long products, in: Darmstadt, 2018.
- [21] A. Borowikow, H. Blei, Integration of Screw Rolling in the Thermo-Mechanical Treatment of Steel Bars, *Roll Pass Des.* 72 (2011) 53–60.
- [22] S.P. Galkin, B.A. Romantsev, A. Borowikow, New inline process for thermomechanical treatment of steel bars, *CIS Iron Steel Rev.* 1 (2012). <http://www.rudmet.ru/journal/996/article/15687/> (accessed May 5, 2021).
- [23] M. Lembke, L. Oberli, G. Olschewski, Probing the limits of steel by producing an ultrafine microstructure in a single extreme deformation step, in: Amsterdam-Schiphol, The Netherlands, 2017.
- [24] M. Lembke, Ultrafeinkörnige thermomechanisch behandelte Langprodukte mit hohen Zähigkeitswerten, in: Dresden, 2017.
- [25] ASTM, ASTM 647-15 Test Method for Measurement of Fatigue Crack Growth Rates, ASTM International, n.d. <https://doi.org/10.1520/E0647-15E01>.
- [26] E.M. Lehigh, Y.-P. Lin, O.E. Lepik, Mapping Residual Plastic Strain in Materials Using Electron Backscatter Diffraction, in: A.J. Schwartz, M. Kumar, B.L. Adams (Eds.), *Electron Backscatter Diffraction*, Mater. Sci., Springer US, Boston, MA, 2000: pp. 247–264. [https://doi.org/10.1007/978-1-4757-3205-4\\_20](https://doi.org/10.1007/978-1-4757-3205-4_20).
- [27] L. Zhao, N.H. van Dijk, E. Brück, J. Sietsma, S. van der Zwaag, Magnetic and X-ray diffraction measurements for the determination of retained austenite in TRIP steels, *Mater. Sci. Eng. A* 313 (2001) 145–152. [https://doi.org/10.1016/S0921-5093\(01\)00965-0](https://doi.org/10.1016/S0921-5093(01)00965-0).
- [28] J. Gussone, K. Bugelnig, P. Barriobero-Vila, J.C. da Silva, U. Hecht, C. Dresbach, F. Sket, P. Cloetens, A. Stark, N. Schell, J. Haubrich, G. Requena, Ultrafine eutectic Ti-Fe-based alloys processed by additive manufacturing – A new candidate for high temperature applications, *Appl. Mater. Today* 20 (2020) 100767. <https://doi.org/10.1016/j.apmt.2020.100767>.
- [29] R. Petrov, L. Kestens, A. Wasilkowska, Y. Houbaert, Microstructure and texture of a lightly deformed TRIP-assisted steel characterized by means of the EBSD technique, *Mater. Sci. Eng. A* 447 (2007) 285–297. <https://doi.org/10.1016/j.msea.2006.10.023>.

- [30] C.O.A. Semprimoschnig, J. Stampfl, R. Pippan, O. Kolednik, A New Powerful Tool for Surveying Cleavage Fracture Surfaces, *Fatigue Fract. Eng. Mater. Struct.* 20 (1997) 1541–1550. <https://doi.org/10.1111/j.1460-2695.1997.tb01509.x>.
- [31] Y.J. Park, I.M. Bernstein, The process of crack initiation and effective grain size for cleavage fracture in pearlitic eutectoid steel, *Metall. Trans. A.* 10 (1979) 1653–1664. <https://doi.org/10.1007/BF02811698>.
- [32] Y. Estrin, A. Vinogradov, Fatigue behaviour of light alloys with ultrafine grain structure produced by severe plastic deformation: An overview, *Int. J. Fatigue.* 32 (2010) 898–907. <https://doi.org/10.1016/j.ijfatigue.2009.06.022>.
- [33] K. Hockauf, M.F.-X. Wagner, T. Halle, T. Niendorf, M. Hockauf, T. Lampke, Influence of precipitates on low-cycle fatigue and crack growth behavior in an ultrafine-grained aluminum alloy, *Acta Mater.* 80 (2014) 250–263. <https://doi.org/10.1016/j.actamat.2014.07.061>.
- [34] M. Arzaghi, C. Sarrazin-Baudoux, J. Petit, Fatigue Crack Growth in Ultrafine-Grained Copper Obtained by ECAP, *Adv. Mater. Res.* 891–892 (2014) 1099–1104. <https://doi.org/10.4028/www.scientific.net/AMR.891-892.1099>.
- [35] T. Niendorf, F. Rubitschek, H.J. Maier, D. Canadinc, I. Karaman, On the fatigue crack growth–microstructure relationship in ultrafine-grained interstitial-free steel, *J. Mater. Sci.* 45 (2010) 4813–4821. <https://doi.org/10.1007/s10853-010-4511-7>.
- [36] H.-K. Kim, M.-I. Choi, C.-S. Chung, D.H. Shin, Fatigue properties of ultrafine grained low carbon steel produced by equal channel angular pressing, *Mater. Sci. Eng. A.* 340 (2003) 243–250. [https://doi.org/10.1016/S0921-5093\(02\)00178-8](https://doi.org/10.1016/S0921-5093(02)00178-8).
- [37] T. Niendorf, D. Canadinc, H.J. Maier, Fatigue Damage Evolution in Ultrafine-Grained Interstitial-Free Steel, *Adv. Eng. Mater.* 13 (2011) 275–280. <https://doi.org/10.1002/adem.201000272>.
- [38] F.D. Fischer, Q.-P. Sun, K. Tanaka, Transformation-Induced Plasticity (TRIP), *Appl. Mech. Rev.* 49 (1996) 317–364. <https://doi.org/10.1115/1.3101930>.
- [39] V. Wirths, W. Bleck, T. Melz, Prozessführung und zyklisches Werkstoffverhalten von karbidfreien bainitischen Stählen, Dissertation, Rheinisch-Westfälische Technische Hochschule Aachen, 2016, 2017. <https://publications.rwth-aachen.de/record/678237> (accessed May 5, 2021).
- [40] V. Wirths, W. Bleck, R. Wagener, T. Melz, Bainitic forging steels, in: 2014.
- [41] V. Wirths, W. Bleck, R. Wagener, T. Melz, Carbide free bainitic forging steels with improved fatigue properties, in: 2015.
- [42] V. Wirths, W. Bleck, R. Wagener, T. Melz, Forging steels with carbide free bainite for high service fatigue life properties, in: 2014.
- [43] V. Wirths, L. Elek, Schmiedestähle mit verbesserter Betriebsfestigkeit durch verformungsinduzierte Phasenumwandlung, Forschungsgesellschaft Stahlverformung e.V, Hagen, 2014.
- [44] V. Wirths, R. Wagener, W. Bleck, T. Melz, Bainitic Forging Steels for Cyclic Loading, *Adv. Mater. Res.* 922 (2014) 813–818. <https://doi.org/10.4028/www.scientific.net/AMR.922.813>.
- [45] J. Wang, P.J. Van Der Wolk, S. Van Der Zwaag, On the influence of alloying elements on the bainite reaction in low alloy steels during continuous cooling, *J. Mater. Sci.* 35 (2000) 4393–4404. <https://doi.org/10.1023/A:1004865209116>.
- [46] J. Wang, S. Van Der Zwaag, Stabilization mechanisms of retained austenite in transformation-induced plasticity steel, *Metall. Mater. Trans. A.* 32 (2001) 1527–1539. <https://doi.org/10.1007/s11661-001-0240-5>.

- [47] D. Broek, *The Practical Use of Fracture Mechanics*, Springer Netherlands, 1988.
- [48] T.B. Hilditch, I.B. Timokhina, L.T. Robertson, E.V. Pereloma, P.D. Hodgson, Cyclic Deformation of Advanced High-Strength Steels: Mechanical Behavior and Microstructural Analysis, *Metall. Mater. Trans. A*. 40 (2009) 342–353. <https://doi.org/10.1007/s11661-008-9732-x>.
- [49] G.K. Tirumalasetty, M.A. van Huis, C. Kwakernaak, J. Sietsma, W.G. Sloof, H.W. Zandbergen, Deformation-induced austenite grain rotation and transformation in TRIP-assisted steel, *Acta Mater.* 60 (2012) 1311–1321. <https://doi.org/10.1016/j.actamat.2011.11.026>.

## Highlights

- We have produced an ultrafine-grained micro-bainitic TRIP-assisted steel
- TRIP effect occurs despite of significant austenite grain refinement of the new steel
- The higher residual austenite content improves the resistance to crack growth

## **Declaration of competing interest**

The authors declare that they have no known competing financial interests or personal relationships that could have appeared to influence the work reported in this paper

## Supplementary figures



Figure S1: Samples taken to determine the austenite and martensite phase fractions at different radii in the unstrained sample.

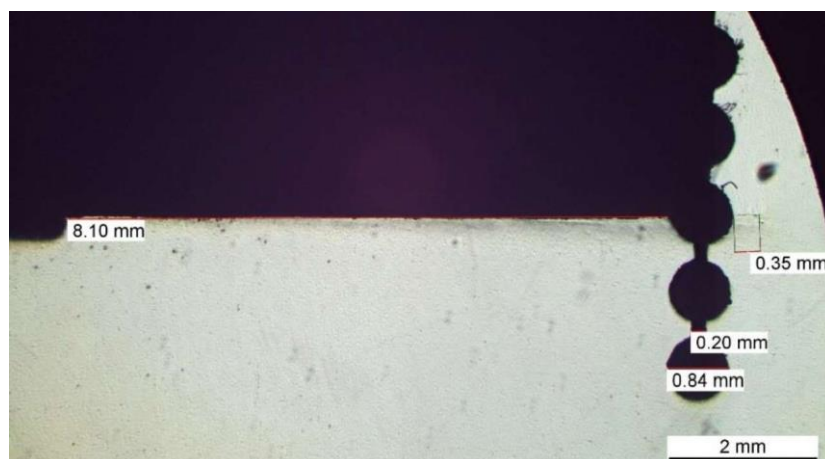


Fig. S2: 5 Samples were cut out of the TM sample with a crack length of around 8mm by discharge machining. Reference samples where no TRIP effect is expected are taken at the sides of the crack tip equidistantly with 1mm spacing. For the STD material 3 samples were cut out similar to the TM material.



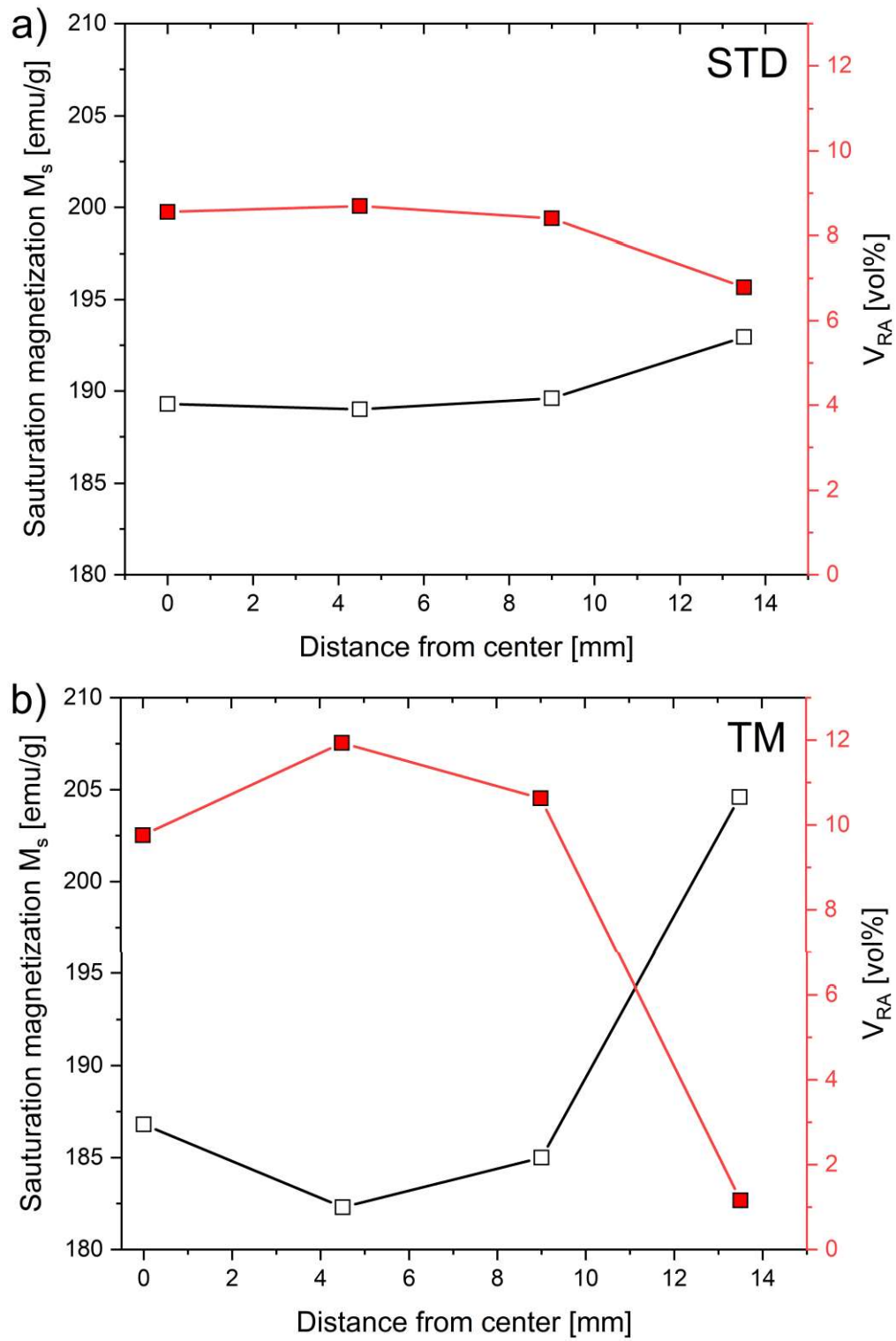


Figure S3: Residual austenite at different radii from the center. 0 is the center of the bar, while 14 mm is at the outside of the bar. The amount of Residual austenite was calculated using a saturation magnetization of 207 emu/g.